MCP RESEARCH ARTICLE COLLECTION: SINGLE-CELL PROTEOMICS

Cell-State-Specific Drug Responses are Associated With Differences in Signaling Network Wiring

Authors

Niels Krämer, Roderick van Eijl, Tim Stohn, Sabine Tanis, Lodewyk FA. Wessels, Evert Bosdriesz, and Klaas W. Mulder

Correspondence

e.bosdriesz@vu.nl; k.mulder@science.ru.nl

In Brief

Not all cells in a population respond the same to external signals or drug treatment, suggesting cell-to-cell differences in signal processing. These cellular responses depend on how the signal flows through the intracellular biochemical networks to eventually regulate transcription factors. Using (phospho-)protein measurements from individual cells and computational modelling, we found that targeting downstream effectors of the EGFR pathway results in redirected signaling flow and that the paths available in the signaling network depend on the underlying state of the cell.

Graphical Abstract

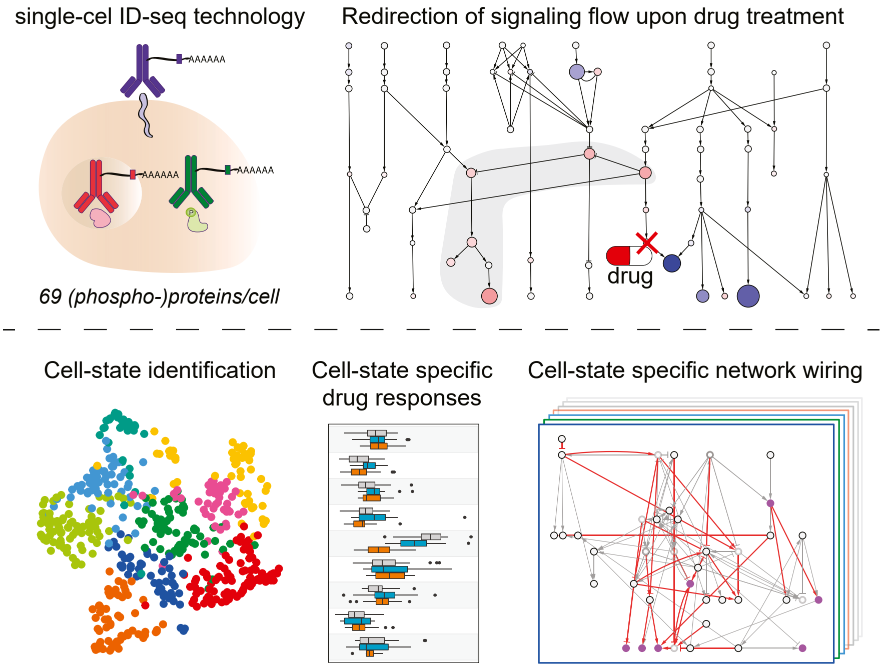

Highlights

- We study signaling response to drug treatment in individual cells using scID-seq.
- Inhibition of downstream effectors results in redirection of signaling flow.
- The state of the cell influences the response to inhibitor treatment.
- Computational reconstruction indicates cell-state-specific signaling network wiring.

2026, Mol Cell Proteomics *25*(*3*), 101529

https://doi.org/10.1016/j.mcpro.2026.101529

Cell-State-Specific Drug Responses are Associated With Differences in Signaling Network Wiring

Niels Krämer[1,‡], Roderick van Eijl[1,‡], Tim Stohn[2,3], Sabine Tanis[1], Lodewyk FA. Wessels[3], Evert Bosdriesz[2,‡*], and Klaas W. Mulder[1,‡*]

Intracellular signaling pathways form networks through which information is transmitted, often in the form of kinase-mediated phosphorylation events, to interpret extracellular signals and elicit appropriate cellular responses. Yet, even isogenic cells in a homogenous environment show heterogeneity in their intracellular "cell-state", as well as their response to extracellular signals. Here, we aimed to better understand this relation between these phenomena by investigating how information flows through the EGF-receptor centered network upon targeted drug treatment, and how this is affected by cell-to-cell-state differences. Using single-cell ID-seq, we profiled the cell-state and signaling activity in primary human epidermal stem cells by measuring 69 (phospho-)proteins upon inhibition of the Erk/MAPK (p90RSK) and Akt/mTOR (p70S6K) routes downstream of the EGF pathway. We found that the effects of drug treatment propagated from the EGF-signaling pathway to other connected parts of the cellular signaling network, indicating altered signaling flow. We identified nine distinct cell-states that show pervasive state-dependent drug-responses for many (phospho-)proteins. Computational modeling of the signaling network using single-cell Comparative Network Reconstruction showed that many interactions between phospho-proteins (i.e. network wiring) were quantitatively different between cell-states. Furthermore, (phospho-)proteins with a cell-state dependent drug response, were more likely to be involved in interactions that showed a cell-state dependent strength. Overall, our results indicate that drug treatment response and signaling interactions between proteins are closely related and modulated by cell-state.

Cells in the human body constantly receive signals from their environment and have to translate these cues into appropriate cellular responses. Yet, what determines how a cell will react to a signal is still poorly understood. Many of the major communication signals that cells use are recurrent throughout embryonic development and normal physiology and are frequently mis-regulated in disease. In each of these biological contexts, these signals can have very different, even opposing, consequences. Cellular responses start with the interpretation of environmental signals. In many cases, extracellular peptide growth factors bind to a cell's surface receptors, initiating a cascade of phosphorylation events that eventually converge on transcription factors in the nucleus, leading to changes in mRNA expression and thereby cellular functions (1, 2). Inside the crowded environment of the cell, distinct extracellular signals frequently use common effector proteins (kinases) serving as intersections (cross-talk points) between pathways. Hence, signaling pathways relaying information through the cell must be approached as complex interconnected networks, rather than isolated silos. A critical implication of this view is that the route the initial signal takes through these networks governs which nuclear factors are impacted and, therefore, the transcriptional response. As such, the "wiring" of this network (e.g., which substrates are available to the activated kinases and their connections) determines the possible paths by which the signal can regulate cellular processes.

Much of our current understanding of signaling pathways and their connectivity is based on cell population averages and qualitative methods. This established epidermal growth factor (EGF) Receptor signaling as an interconnected network of kinases, containing multiple distinct pathways with different functions. The predominant pathways in the EGF signaling network are the Akt-mTOR and Ras/ERK (MAPK) signaling cascades (Fig. 1*A*) (1, 2). Both these signaling routes lead to phosphorylation of ribosomal protein S6 (RPS6), as well as downstream DNA-binding transcription factors (1, 3).

From the [1]Radboud Institute for Molecular Life Sciences, Faculty of Science, Department of Molecular Developmental Biology, Radboud University, Nijmegen, the Netherlands; [2]Department of Computer Science, Vrije Universiteit, Amsterdam, the Netherlands; and [3]Department of Molecular Carcinogenesis, Netherlands Cancer Institute, Amsterdam, the Netherlands and the Oncode Institute

[‡]These authors contributed equally to this work.

*For correspondence: Evert Bosdriesz, e.bosdriesz@vu.nl; Klaas W. Mulder, k.mulder@science.ru.nl.

Present addresses for: Sabine Tanis, Single Cell Discoveries, Utrecht, the Netherlands; Niels Krämer, Karolinska Institutet, Department of Cell and Molecular Biology, Stockholm, Sweden; Roderick van Eijl, Charles River Laboratories, Leiden, the Netherlands.

https://doi.org/10.1016/j.mcpro.2026.101529

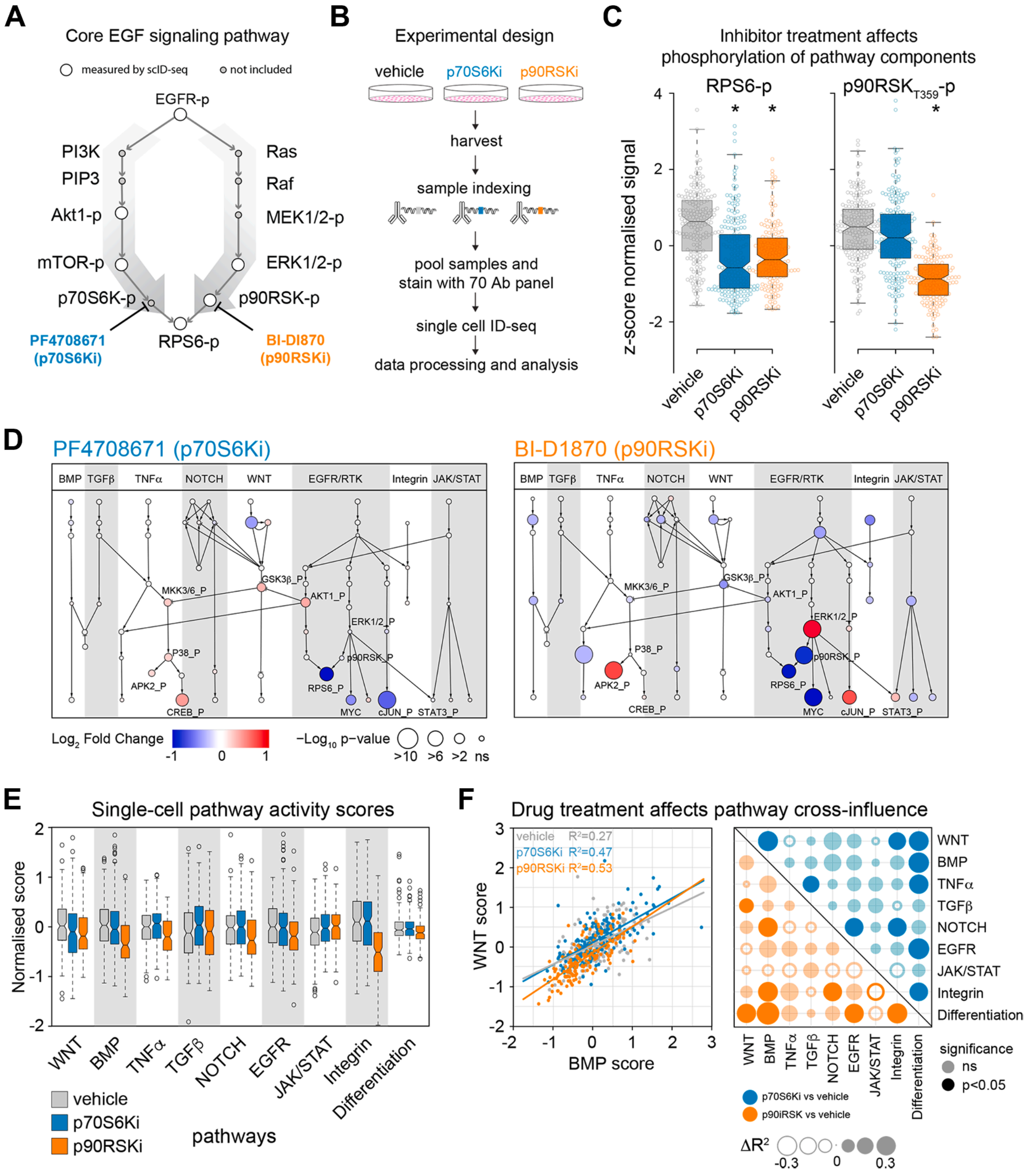

FIG. 1. **Single-cell ID-seq profiling of signaling protein activity shows widespread and heterogeneous response to targeted inhibition.** *A*, schematic overview of the AKT and MAPK signaling pathways. *B*, schematic overview of the scID-seq workflow. *C*, boxplots of phospho-RPS6 (*left*) and phospho-p90RSK abundance upon drug treatment. Abundances are TTM-normalized and subsequently z-score transformed to facilitate comparison. *D*, differential abundance of signaling phospho-proteins upon p70S6Ki (*left*) and RSKi (*right*) shows that treatment effects propagate throughout the signaling network. Colors indicate $\log_2$-fold change, node sizes indicate $-\log_{10}$ *p*-values. Edges between proteins are drawn based on literature-established interactions. *E*, single-cell pathway activity scores upon drug treatment. Pathway activity scores are obtained by combining multiple features that belong to a pathway, accounting for activating or inhibiting effects on the pathway. *F*, drug treatment induces changes in pathway cross-influence. *Left panel*: scatterplot of BMP vs Wnt pathway scores per cell for vehicle and inhibitor treatment conditions. Pathway cross-influence was defined as the coefficient of determination (R^2) of a linear regression model. *Right panel*: Systematic analysis of drug-induced changes in pathway cross-influence. Bubble size is proportional to the difference in R^2 between vehicle and treatment condition, transparency indicates statistical significance, closed and open circles represent increase and decrease, respectively.

For instance, the p90RSK kinase activates RPS6 downstream of MAPK signaling through Erk1/2, whereas p70S6K phosphorylates RPS6 upon activation by Akt-mTOR (2). Importantly, many potential points of cross-talk and feedback have been described between EGF- and other signaling pathways. This is exemplified by the inactivating phosphorylation of Wnt-pathway component GSK3β (on Serine 9) by Akt/PKB (1, 2), and activation of JAK-STAT signaling component STAT3 via RAS/ERK signaling (4). Recent years have seen advances in studying signaling dynamics using single-cell approaches. For instance, mass cytometry analysis of overexpressed GFP-tagged kinases revealed an interdependence of kinase effector abundance and the dynamics of signaling progression through the EGFR pathway (5, 6). Additionally, optogenetic activation of Son-of-Sevenless (SOS) allowed quantitative screening of drug treatment-effects on the Erk/MAPK-pathway, demonstrating that targeted drugs can corrupt its dynamic signal-transmission properties in a potentially pathological manner (7).

Cancer-associated mutations are often found in components of key developmental signaling pathways, which has led to a great interest and investment in developing small molecule drugs against specific kinases to block these cancer-driving pathways (8, 9). Although promising and powerful, the emergence of drug resistance is a major problem in current clinical practice (10–13). Identified drug resistance mechanisms include the selection/appearance of cells with desensitizing genetic mutations, as well as the existence of seemingly mutation-independent stochastic drug-tolerant cell states (14–17). A common denominator of drug resistance mechanisms is that the way the extracellular signals are perceived and processed is changed to benefit the resistant cell, indicating that variation in the signaling network can greatly impact the cellular outcome. The observation that even within seemingly homogenous cell populations, not all cells respond in the same way, suggests that intrinsic (or “cell-state”) differences between cells influence their response (18, 19). Cell-states include, for instance, the combination of prior and current signaling events, cell cycle status, differentiation level and position with respect to other cells. Indeed, decades-old observations indicate that cells experimentally arrested in distinct phases of the cell cycle exhibited different activity of downstream effectors of the EGFR (20, 21). However, how the internal state of a cell affects the flow of information inside the cell and the subsequent transcriptional response is still largely unknown. Considering that the response of a given cell to an environmental signal is inherently cell-autonomous (i.e. it is determined by intracellular molecular mechanisms), the processes involved must be studied at the level of individual cells.

Here, we describe the use of cultured primary human epidermal keratinocytes to study drug responses at the resolution of individual cells using single-cell ImmunoDetection-by-sequencing (scID-seq) to measure ~70 (phospho-)proteins per cell in different conditions. Using the core Epidermal Growth Factor Receptor signaling pathway as a paradigm, we found that blocking down-stream pathway effectors p90RSK and p70S6K resulted in cell-state-dependent signaling responses. Using a newly developed single-cell comparative network reconstruction (scCNR) model, we identified the differences in signaling network wiring associated with these cell-states.

EXPERIMENTAL PROCEDURES

Cell Culture

Primary pooled human epidermal stem cells derived from foreskin were obtained from Lonza. Cells were cultured and expanded as previously reported (22). Briefly, cells were cultured on a feeder layer of J2-3T3 cells in FAD medium (Ham’s F12 medium/Dulbecco’s modified Eagle medium (DMEM) (1:3) supplemented with 10% batch tested fetal calf serum (FCS) and a cocktail of 0.5 μg/ml of hydrocortisone, 5 μg/ml of insulin, 0.1 nM cholera enterotoxin, and 10 ng/ml of epidermal growth factor) supplemented with Rock inhibitor (Y-27632, 10 μM). J2-3T3 cells were cultured in DMEM containing 10% bovine serum and inactivated with MitomycinC (SCBT) upon seeding the epidermal stem cells. For experiments epidermal stem cells were transferred to Keratinocyte Serum Free Medium (KSFM) supplemented with 0.2 ng/ml epidermal growth factor (EGF) and 30 μg/ml bovine pituitary extract from Life Technology until 70% confluency. Cells were treated with p90RSK inhibitor BI-D1870 (10 μM, Sellekchem) or P70S6K inhibitor PF4708671 (10 μM, Sellekchem). All media were supplemented with 1% penicillin/streptomycin antibiotics. We included a non-stimulated control and found that endogenous EGFR ligands produced by the cells themselves circumvented the need for exogenous pathway activation (data not shown). Although this control group was omitted from further analyses, these measurements are included in the full dataset.

Antibody Conjugation With dsDNA Barcodes

The antibody panel, including extensive validation, dsDNA functionalization and conjugations were performed as described (23–25). In short, antibodies were functionalized with NHS-s-s-PEG4-tetrazine (Jena Bioscience) in a ratio of 1:10 in 50 mM borate buffered Saline pH 8.4 (150 mM NaCl). Then, N3- dsDNA was produced and functionalized with DBCO-PEG12-TCO (Jena Bioscience) in a ratio of 1:25. Finally, purified functionalized antibodies were conjugated to purified functionalized DNA by 4-h incubation at room temperature in borate buffered saline pH 8.4 in a ratio of 4:1 respectively. The reaction was quenched with an excess of 3,6-diphenyl tetrazine. The conjugation efficiency and quality were confirmed on an agarose gel, and equal amounts of each conjugate were pooled for scID-seq experiments. The antibodies used in this study and their associated DNA barcodes are listed in Table S6.

Immuno-Staining and Single Cell Sorting

Staining and sorting was performed as described previously. Briefly, Cells (>3 × 10^6) were harvested with trypsin and cross-linked in suspension by incubating for 10 min with 4% paraformaldehyde (PFA) in PBS following a quenching step of 5 min with 125 mM Glycine in PBS. Removal of PFA and Glycine occurred through washing twice with a wash buffer (0.1× Pierce Protein-Free Blocking Buffer from Thermo in PBS). Then, cells were blocked in 500 μl blocking buffer (0.5× Pierce Protein-Free Blocking Buffer, 200 μg/ml boiled salmon sperm DNA, 0.1% Triton-X 100, in PBS) at room temperature for 30 to 60 min. Pre-stainings were performed at room temperature for 1 to 2 h, and staining with the conjugate mix occurred overnight at 4 °C in 500 µl blocking buffer. After each staining, cells were washed 3× in 5 ml wash buffer. Cells were sorted in single wells with the BD FACSAria SORP flow cytometer (BD Biosciences) in 96-well PCR plates containing 1 µl release buffer (10 mM DTT in 15 mM Tris, pH 8.8) and 7 µl Vapor-lock (Qiagen).

Barcoding and Library Preparation for Next-Generation Sequencing

scID-seq—Library preparation was performed as described previously (24). Briefly, 3 PCR steps were performed to amplify the antibody barcodes and to add barcodes specific for the well and the plate of each cell. The barcoding occurred with the same sequences used in ID-seq (23). For the first PCR step 15 cycles were run after adding to each well a 4 µl reaction mix containing the Herculase II Fusion DNA Polymerase (Agilent), dNTPs, 5× Herculase buffer and 0.1 µM amplification primers. Directly after the first PCR step, 5 extra cycles were run after adding 1 µl mix containing Herculase buffer 0.2 µM forward amplification primer and 0.2 µM reverse well barcoding primer. Then all material was pooled per plate, Vapor-lock was removed and a clean-up was performed with the QIAquick PCR Purification Kit, followed by an exonuclease 1 treatment to degrade remaining primers and another purification. Another 5 cycles were run in PCR 3 with a 20 µl reaction containing the pooled and purified sample and 0.1 µM plate-barcoding primers. After repeating the clean-up procedure, the libraries were checked on agarose gel and with the Bioanalyzer (Agilent) to confirm the size of the DNA fragments (expected size around 185 bp) and sequenced on an Illumina NextSeq500 machine.

scRNA-seq—Library preparation was performed as described previously (26). Briefly, cultured cells were dissociated, followed by fixation with 2.5 mM DSP and 2.5 mM SPDP in sodium phosphate buffered saline (pH 8.4) for 45 min at RT in order prevent transcriptional changes during the single-cell sorting, The fixation was quenched by adding 100 mM Tris-HCl pH 7.5 and 150 mM NaCl for 10 min. Individual cells were sorted (BD FACS Aria) into 384-well plates containing CEL-seq2 primers. The cDNA library preparation was adapted from the previously published protocol (26), and the ERCC spike-in (1:100,000 dilution, Thermo Fisher Scientific) was added to the reverse crosslinking mix. The cDNAs were selected using a 0.6× Ampure XP bead ratio (Beckman Coulter) purification and subsequently subjected to second-strand synthesis and subjected to *in vitro* transcription-based amplification using Megascript T7 transcription kit (Thermo Fisher Scientific). The amplified RNA was subjected to reverse transcription, PCR amplified followed by Illumina index addition to create the final sequencing library.

Data Preprocessing

scID-seq—Sequence data from the NextSeq500 (Illumina) was demultiplexed using the bcl2fastq software (Illumina). Then, all reads were processed using our dedicated IDseq R-package (23). In short, the sequencing reads were split using a common "anchor sequence" identifying the position of the Unique Molecular Identifier (UMI) sequence, Barcode 1 (antibody specific) and Barcode 2 (well specific) sequence. After removing all duplicate reads, the number of UMI sequences was counted per Barcodes 1 and 2. Finally, Barcode 1 ("antibody)" and Barcode 2 ("well") sequences were matched to the corresponding antibody and well information.

Next, cell and antibody outliers were removed from the data. Specifically, cells with a total UMI-corrected count number of <25,000 or a median antibody count of <100 were removed. Cells were also removed if one or more antibodies had a UMI count >5 standard deviations above the population mean. Finally, antibodies with a median UMI count <40 were removed.

Antibody counts were normalized through TMM-normalization by, for each cell, scaling all counts with a normalization factor corrected library size. The normalization factors were calculated with the function *calcNormFactors* from the edgeR R-package (27) using the parameters sumTrim = 0.05 and logratioTrim = 0. Plate effects were corrected using the function *removeBatchEffect* from the limma R-package (28) using the plate number as batch indicator.

scRNA-seq—The sequence data were demultiplexed using bcl2fastq software (Illumina). RNA sequence data were processed using CELseq2 pipeline (29), which includes demultiplexing based on cell barcodes, mapping to GRCh38 using Bowtie2 (30) and UMI counting by HTseq. The processed sequencing data were analyzed using the Seurat V4 package.

Cell-State Cluster Assignment—To exclude treatment effects from affecting the clustering, clustering was performed only on so-called *cell-state markers*, i.e. (phospho-)proteins that are not significantly differentially abundant between treatments (Kruskal-Wallis test, comparing vehicle with p70S6Ki and p90RSKi, -log10 *p*-value <5) as previously described (18). Next, the TMM normalized data were z-score normalized on a per-(phospho-)protein basis to ensure equal contribution between (phospho-)proteins with high and low average number of counts. The z-score normalized data were transformed into an adjacency matrix using a shared nearest neighbor approach as implemented in the 'RANN' package (https://jefferislab.github.io/RANN/), using k = 15.

Robust and reproducible "consensus" cell-state clusters were identified based on repeated application of the Leiden algorithm (31). The Leiden algorithm was run (with a resolution of 1.2) until it reached a stable configuration 1000 times. While the number of identified clusters varied from seven to 12, approximately 70% of the runs resulted in nine clusters. To facilitate the determination of the consensus clusters, we filtered out all iterations of the Leiden algorithm where the number of clusters was different from nine. Next, a co-occurrence distance matrix of cells was calculated using the *cooccur* function from the 'kmed' package (32). Finally, hierarchical clustering on the co-occurrence matrix and cutting the resulting dendrogram with k = 9 using the base R function *cuttree* resulted in nine consensus clusters.

To assess the reproducibility of this pipeline, it was repeated 5 times. The vast majority of cells were consistently assigned to the same cluster in all 5 repeats. The 12 cells where this was not the case were marked as assigned to the cluster they occurred in most (in all cases, 4/5 times) but marked as "ambiguous".

Cell-State Cluster Classifiers—Multinomial Logistic Regression (MLR), Random Forest (RF), and Support Vector Machine (SVM) classifiers were trained to assign cells to one of the 9 cell-state clusters. The classifiers were trained on the cell signaling markers, which were not considered in the cluster assignment. In addition, as positive control models to predict the cell-states from the cell-state markers were trained. The classifiers used the z-score scaled protein counts of the TMM normalized data as input. The classifiers were evaluated using a nested cross-validation scheme with a five-fold inner and five-fold outer loop. This procedure was repeated five times. The Random Forest was optimized using randomly selected predictors (possible values 2, 5, 10), number of trees (possible values 500, 1000, 2000), and minimal node size (possible values 2, 5, 10) by exhaustively testing all parameter combinations in the nested cross-validation scheme. For the MLR model the penalty and model type were optimized and for the SVM the cost and sigma parameter. The MLR and SVM model parameters were tuned over a grid with 50 random parameter combinations.

Pathway Activity Score—To calculate the pathway activity scores, the TMM normalized data were z-score transformed so that each (phospho-)protein has the same weight when contributing to a particular score. To account for whether a factor/phosphorylation event activates or inhibits pathway activity, each (phospho-)protein was assigned to have a positive (+1), a negative (−1), or no (0) contribution to the score of each pathway (Table S5). We confirmed that the variance of the pathway scores does not systematically depend on the number of antibodies that it consists of (Fig. S9). R^2-values were calculated for each treatment separately using Pearson correlation between each pathway pair and taking the square. Empirical *p*-values for the differences in R^2 between treatments were calculated by randomly permuting the treatment labels and recalculating the R^2 for each treatment. This was repeated 10,000 times to obtain a null-distribution for the difference in R^2 between control and each treatment condition.

Identification of Cell-State-Specific Drug Response—Cell-state-specific drug responses were identified by regressing the expression of each (phospho-)protein a in each cell *i*, $E_{i,a}$, to the drug-treatment T_i and cell-state S_i, and include an interaction term, i.e. the following linear model was used for each (phospho-)protein using the base R function ‘lm’.

$$E_{i,a} \sim \beta_{0,a} + \beta_{T,a} \cdot T_i + \beta_{S,a} \cdot S_i + \beta_{I,a} \cdot T_i \cdot S_i$$

In the design matrix, vehicle treatment and cell-state 1 were used as reference states. Significance was assessed using a two-way ANOVA using the base R function ‘aov’. In addition, the significance of interactions for each cell-state-treatment combination individually was assessed using the *p*-values, and the interaction coefficients $\beta_{I,a}$ was used. Multiple testing correction was performed using the Benjamini-Hochberg procedure as implemented in the base R function *p.adjust*.

Single-Cell Comparative Network Reconstruction—A full description of the single-cell Comparative network reconstruction, including derivation of the underlying equations and validation on simulated and real data, is published elsewhere (33). Briefly, scCNR is a reformulation of our previous Comparative Network Reconstruction algorithm (34) that aims to quantify the interaction strengths r^{ξ}_{ij} between the all protein pairs *i* and *j* in a signaling network, and how these differ between cell-states ξ. To this end, it exploits the stochastic variation in total and phospho-protein abundances. In a first order Taylor series, the deviation from the cell-state population mean of the activity and total abundance of protein *i* in cell *a*, $R_{i,a}$ and $R^{tot}_{i,a}$ respectively, the sensitivity of the activity of protein *i* to changes in its total abundance, s^{ξ}_i, the effect of drug treatment *m*, p^{ξ}_{im}, and the interaction strengths between proteins are related through the set of linear equation, one for each node in each cell:

$$R_{ia} \approx \sum_{j/=i} r^{\xi}_{ij} \cdot R_{j,a} + s^{\xi}_i \cdot R^{tot}_{i,a} + p^{\xi}_{im} \quad \forall a, i, \xi$$

Here, the ξ superscript refers to possible cell-state specific values of the parameters. scCNR solves an optimization problem to find a network (i.e. the values of r^{ξ}_{ij}) that fits these equations well while minimizing model complexity (i.e. the number of protein interaction in the network/nonzero values of r_{ij}) and the number of edges that differ in strength between the cell-states (i.e. have values for which $r^{k}_{ij} \; /= r^{l}_{ij}$ for different cell-states *k* and *l*). The strengths of the penalties on the number of edges in the network and the number of edges that differ in strength between cell-states is set by the hyperparameters η and θ, respectively. Prior information about the presence or absence of interactions can be easily incorporated as additional indicator constraints to the optimization problem, coded for by binary indicator variables I_{ij}.

This optimization problem can be formulated as a Mixed Integer Quadratic Programming (MIQP) problem. The MIQP optimization problem is solved using IBM ILOG CPLEX solver (Version 22.1), which is freely available for academic use. Importantly, it guarantees optimal solutions within small numerical tolerances.

Identification of Model Topology—To reduce the search space, identification of network topology and interactions that differ between cell-states were decoupled. Initially, to obtain a suitable model topology, cell-state information was ignored, and the $R_{i,a}$-values were calculated as the relative deviation in protein activity for the total population median. For nodes for which both the total and the phospho-protein abundances were quantified, the variation in total protein could be explicitly modeled as a perturbation to the node (the $s_i \cdot R^{tot}_{i,a}$-term). For the nodes where we did not measure total protein abundance, we interpret this as an unobserved perturbation, resulting in worse ability to explain the variation in protein activity. To this end, the residuals corresponding to these nodes are downweighted by a factor α, which is set automatically as described in (33). Drug treatments were modeled as negative perturbations to p90RSK (p90RSK inhibition) and RPS6 (p70S6K inhibition, as p70S6K is not measured itself).

A network of 65 canonical interactions and interactions obtained from PhosphositePlus (35) was included as prior information by adding indicator constraints of the form $I_{ij} = 1$, one for each edge in the starting network, to the optimization problem. Next, edges to be added to the network model were identified by solving optimization problem using $\eta = 0.06$ as this gave a good balance between model fit (as quantified by the RMSR and complexity, Fig. S8*B*), ignoring cell-state information. This way, 34 edges are added to the model, resulting in a final model topology of 42 nodes and 99 edges.

The quality of the model topology obtained was assessed by comparing it to the fit obtained by 500 models with a random network topology. To this end, random models of the same complexity (i.e. 99 edges) were created by randomly setting 99 indicators $I_{ij} = 1$ and all others indicators to 0. By solving the MIQP optimization problem under these constraints, the interaction strengths and thus also RMSRs of these models were obtained. These could then be compared to the RMSR from the actual model (Fig. 4*B*).

Identification of Cell-State-Specific Edge Strengths—To identify which edges differ between the cell-states, scCNR with cell-state information included was run. To this end, the input values of $R_{i,a}$ and $R^{tot}_{i,a}$ were calculated as the relative deviation in protein activity from the cell-state median. The network topology as obtained above was provided by setting the 99 indicators corresponding to included edges to 1 and all other indicators to 0. The hyperparameter penalizing differences between cell-states, θ, was set to 0.2 as this gave a good balance between the number of differences between the networks and the reduction in RMSR (Fig. S8*C*). Otherwise, the optimization was run as described above. This resulted in a network with 34 differences between the networks: 31 of the differences were edges, 2 differences in sensitivity to the total protein abundance, and 1 a difference in the direct effect of a drug treatment on its target.

The bootstrap analysis to assess the robustness of differing edge detection (Fig. S8*D*) was performed by randomly sampling 546 cells (i.e. the original number of cells) *with* replacement and rerunning the MIQP optimization again with $\theta = 0.2$ (i.e. the original value). This procedure was repeated 100 times. From this, the fraction of bootstraps in which an edge is predicted to be cell-state specific can be obtained.

The permutation analysis to assess the statistical significance of edge strength deviations (Fig. 4, *D* and *E*, and Table S4) was performed by randomly shuffling cell-state labels. To ensure an identical distribution of cell-states across treatments, this was done for each treatment separately. Next, the cell-state median and $R_{i,a}$ values were recalculated. The model topology and the edges that differ were all fixed by constraining all indicator variables to be the value they had in the original model. Subsequently, the MIQP optimization was run to obtain the edge strengths for the permuted data. This was repeated 1000 times to obtain a null-distribution of edge-strength-deviation from the population mean.

Enrichment Analyses—For the enrichment analyses presented in Figures 4*H* and S8*E*, we considered all nodes with a significant interaction term according to the ANOVA analysis (Table S3) and edges that are identified as having cell-state-specific interaction strengths in the general scCNR optimization, to obtain the contingency tables. Odds ratios and *p*-values were calculated using one-sided Fisher Exact tests. For the cell-state resolved enrichment analysis, we considered all node-cell-state pairs that have a significant coefficient for their interaction term in the regression analysis (using cell-state 1 as reference), and all edge-cell-state pairs where the deviation in interaction strength significantly differed from the null-distribution obtained from the cell-state label permutation analysis. This way, we obtained the contingency for edge and node enrichment, respectively. Odds ratios and *p*-values were calculated using one-sided Fisher Exact tests.

RESULTS

Single-Cell (Phospho-)Protein Profiling of the Response to p90RSK and p70S6K Inhibition

We used primary human foreskin keratinocytes as a karyotypically normal and genetically stable cell system for our experiments to avoid confounding effects of heterogeneity with respect to cancer-associated mutations in signaling components. To capture how signals are processed and how cells respond to perturbations, we subjected keratinocytes to short-term inhibition of key effectors of the MAPK and AKT-mTOR pathways downstream of the EGFR (Fig. 1*A*). We reasoned that focusing on early effects would allow us to associate pre-existing cell-to-cell heterogeneity with differential cellular responses.

Keratinocytes were grown in medium without exogenous EGF for 24 h prior to the experiment, in which we treated the cells for 2 h with an inhibitor of p90RSK (BI-D1870, 10 μM) or p70S6K (PF4708671, 10 μM), or a vehicle control (DMSO), followed by a 30-min stimulation with 10 ng/ml EGF while maintaining the presence of the inhibitors. After harvesting and fixation, we applied scID-seq to measure the abundance of ~70 (phospho-)proteins in each cell using specific DNA-barcoded antibodies. Our panel contains characterized and validated antibodies detecting phosphorylated and non-phosphorylated components from the Akt-mTOR signaling and MAPK signaling, as well as other key developmental and cancer related pathways (Wnt, BMP, TNFα, TGFβ, Notch, Jak/STAT, and Integrin-mediated adhesion) and cellular processes including the cell cycle and differentiation (23, 24, 36). We used cell-hashing (37) as a sample barcoding approach to minimize batch-effects and variation in staining efficiencies between conditions (Fig. 1*B* and Table S1). After pooling the samples and staining with the full antibody panel, individual cells were distributed into 96-well plates using FACS, effectively randomizing the treatment groups over the different independent sample preparations that are performed per plate. After sequencing, quality control, pre-processing and filtering (see Methods section for more information), we obtained a dataset consisting of 69 (phospho-)protein measurements from 546 cells (Table S1).

Drug Treatment Leads to Alternative Signaling Flow and Transcriptional Responses

Consistent with their known function of phosphorylating RPS6, inhibition of either p90RSK (BI-D1870) or p70S6K (PF4708671) resulted in pronounced reduction of phospho-RPS6 levels, whereas p90RSK-T359 phosphorylation specifically decreased upon p90RSK inhibition, providing confidence in our experimental set-up and scID-seq measurements (Fig. 1*C*). Inspection of further core EGFR pathway components revealed that ERK1/2 and AKT1 phosphorylation signals increased upon p90RSK and p70S6K inhibition, respectively (Fig. S1*A*). This is consistent with their involvement in a regulatory negative feedback loop, a well-known design principle to control signaling pathway activity (38, 39), and raises the question whether these perturbation effects propagate through the wider signaling network through so-called signaling cross-talk. Differential abundance analysis revealed significant changes in (phospho-)protein levels for multiple components of the JNK, p38, and Wnt pathways in cells treated with the p70S6K inhibitor (Kolmogorov-Smirnov test, Figs. S1 and S2, and Table S2). Notably, GSK3β Serine-9 phosphorylation, a known pathway cross-talk event catalyzed by Akt (1, 2, 40), was increased. In turn, inactivation of GSK3β was associated with enhanced phosphorylation of MKK3/6 (Figs. 1*D*, S1*A* and S2, see Fig. S3 for all node identities), consistent with previous findings (41, 42). Furthermore, phosphorylation levels of a known downstream effector of MKK3/6, MAPK-p38, and its subsequent targets MAPK-APK2 (henceforth APK2) and the CREB transcription factor (43, 44) were also significantly increased (Figs. 1*D*, S1*A*, S2 and S3). In contrast, p90RSK inhibition stimulated phosphorylation of STAT3 and decreased phosphorylation of Jak1 and STAT1 (Figs. 1*D*, S1*A* and S2, Table S2). Phosphorylation of STAT3 by MAPK signaling was previously described as a cross-talk mechanism (45, 46). Additionally, we found increased phosphorylation of APK2, independent of its canonical upstream kinases MKK3/6 and MAPK-p38 in p90RSK inhibitor treated cells (Figs. 1*D*, S1*A* and S2). Rather, this APK2 phosphorylation may be a consequence of accumulated ERK activity through direct phosphorylation of the Thr334 site on APK2, as previously described (47).

Thus far, we only considered the mean abundance of each (phospho-)protein per treatment, but there is clear within treatment variation among cells (Figs. 1*C*, S1*A* and S2). To investigate the activity of signaling pathways more systematically, we derived aggregated activity-scores for each pathway for each cell (see Methods for details). This confirmed that p70S6K and p90RSK inhibitors indeed differentially affect signaling at the pathway level (Fig. 1*E*).

Although such aggregate scores cannot fully account for all pathway-specific regulatory intricacies and complexities, it does allow us to methodically assess interactions between pathways while extending it to situations where the points of cross-talk within the signaling network are unknown, and/or not directly represented in our measurements. We defined pathway cross-influence as the proportion of the variation *within* a treatment condition in a given pathway (i.e. the response variable) that is explained by the variation in another pathway (i.e. the explanatory variable) by calculating the coefficient of determination (R^2) between pathway scores across individual cells for each of the treatment conditions. For example, the cross-influence of the BMP and Wnt pathways in vehicle-treated cells was $R^2 = 0.27$ (i.e. 27% of variation was explained), whereas this increased to $R^2 = 0.53$ upon p90RSK inhibition, almost doubling the proportion of variation explained (Fig. 1*F*, left panel). We performed this analysis for all pathway combinations, expressed the difference in coefficient of determination between vehicle and treatment (ΔR^2), and calculated the statistical significance of this difference by randomly permuting treatment labels. This revealed a strong and pervasive perturbation-dependent pathway cross-influence (Fig. 1*F*, right panel). Together, these analyses indicate that p70S6K and p90RSK inhibition resulted in accumulated phosphorylation of upstream regulators (Akt and ERK, respectively), leading to widespread propagation of their effects to other pathways within the biochemical signaling network that could shape the cellular response.

A key mechanism by which extracellular signals and their intracellular transduction pathways influence these responses, and consequently the biology of the cell, involves regulating DNA-binding transcription factors. Therefore, a potential consequence of the observed differential cross-talk is that a different complement of transcription factors is regulated, leading to altered transcriptional output. Consistent with this, p90RSK inhibition resulted in differential (phosphorylation) levels of the transcription regulators Myc and c-Jun (Fig. 1*D*). To investigate the consequences on mRNA expression, we treated keratinocyte cultures with the p90RSK inhibitor BI-D1870 (10 μM) for 2 h followed by single-cell RNA-sequencing. After processing and normalization, clustering and t-SNE representation, we found that vehicle and p90RSK inhibitor treated cells separate into distinct groups based on their RNA profiles (Fig. S1*C*). Moreover, c-JUN mRNA levels were increased, consistent with the (phospho-)protein data and the fact that c-JUN engages in an autoregulatory positive feedback loop (48). The early growth response gene 1 (EGR1) transcript, a canonical c-JUN target, is simultaneously upregulated, indicating that c-JUN transcription regulation is affected by p90RSK inhibition. Moreover, differential expression testing between the two treatments and motif analysis identified enrichment of AP1 (c-JUN) and Myc binding sites in promoters of deregulated transcripts (Fig. S1*D*, *left panel*). These observations were confirmed with an independent p90RSK inhibitor (LJH-685, 10 μM, 2 h, Fig. S1*D*, *right panel*). These findings indicate that even though treatment with a drug blocks the intended target, it can result in activation of alternative pathways through the biochemical signaling network, and unintended transcriptional consequences.

Robust Identification of Distinct Cell-State Clusters From scID-seq Data

An important implication of the findings described above is that the route a signal takes through the network is influenced by whether the signal can be efficiently transmitted to the next node (i.e. network wiring), which is in essence the process that was disrupted by the drug treatment. We hypothesized that this wiring may vary depending on which *cell-state* the cells reside in. Such cell-states can include the position in the cell cycle, the degree of differentiation, ongoing or prior signaling events, and other processes. If this hypothesis is correct, this should be reflected as structured cell-to-cell variation in (phospho-)protein levels in our dataset. Indeed, we observed clear effects on the average phosphorylation level that were accompanied by large within-treatment variations for many of the included (phospho-)proteins (Figs. 1*C*, S1*A* and S2), suggesting the existence of multiple cell-states in our data.

Identifying cell-states can be challenging due to confounding effects associated with the applied treatment. Therefore, we needed a way to identify which cells were most similar to each other (i.e. in the same cell-state) *before treatment*. The approach we took was first described by Kramer and Pelkmans (18), and is based on their observation that treatment non-responsive protein markers allow the identification of these common underlying cell-states, without these identifications being dominated by response to the treatments. For this, we defined 23 (phospho-)proteins that did not show strong treatment responses (Kruskal-Wallis test, comparing vehicle with p70S6Ki and p90RSKi, $-\log_{10}$ *p*-value <5, c.f. Table S2) as “cell-state markers”, and designated all other (treatment responsive) (phospho-)proteins “signaling-state markers”. Subsequently, we developed a robust cluster assignment pipeline, based on the Nearest Neighbor (NN)-dependent Leiden clustering algorithm and identified 9 distinct clusters, which were superimposed on a UMAP representation of our scID-seq dataset (Fig. 2*A*) (31). It is important to note that the Leiden algorithm is non-deterministic in nature as it contains a random NN-network initialization step, leading to unstable cluster calling in repeated iterations (Fig. S4*A*). Consequently, cells on the “borders” between clusters can be mis-assigned. To solve this, we adapted the workflow into a consensus/’majority vote’ approach, using 1000 random initializations to identify the most frequently occurring (i.e. stable) number of clusters (Fig. S4*A*). This is then repeated 5 times and the level of

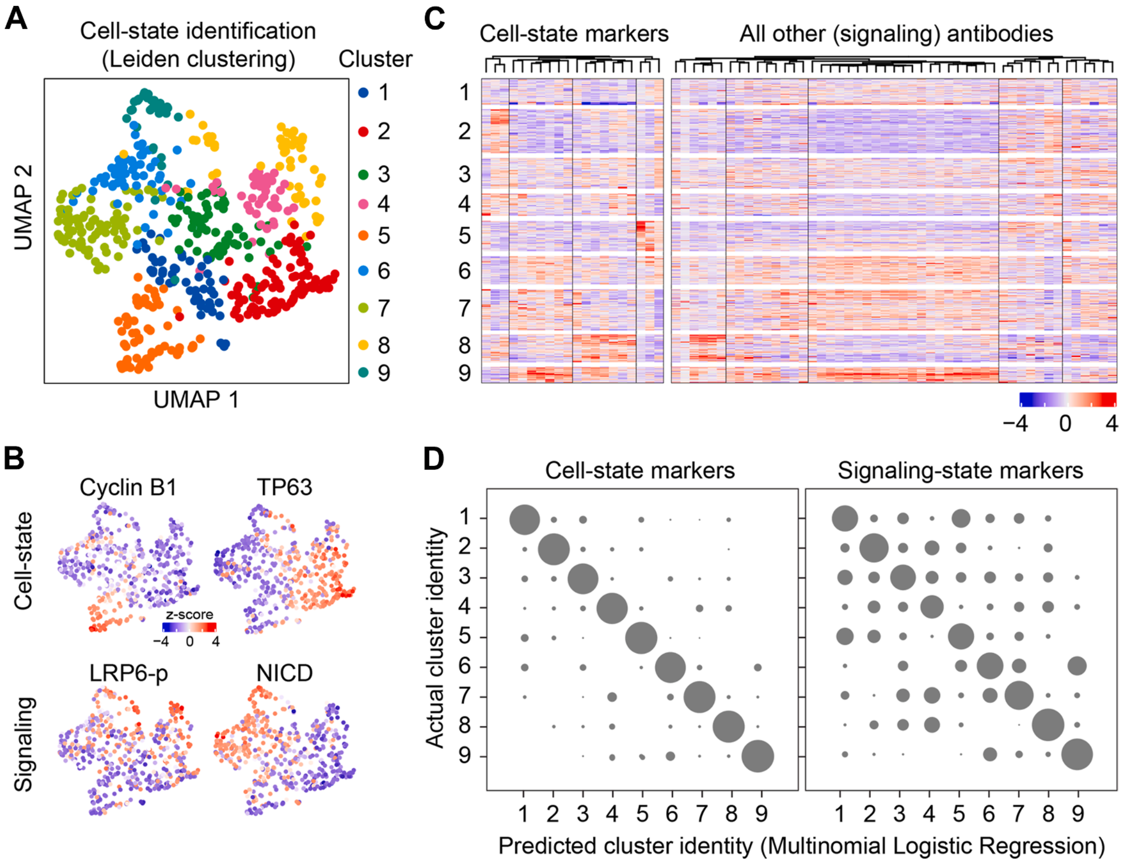

FIG. 2. **Robust identification of nine distinct cell states.** *A*, UMAP projection of the cells, color coded according to their cell-state assignment. Only the cell-state markers (i.e. (phospho-)proteins that did not show a differential abundance between treatments) were used in calculating the UMAP coordinates. *B*, UMAP projection of the cells, color coded by the abundance of selected cell-state (*top* row) or signaling-state (*bottom* row) markers *C*, heatmap of (phospho-)protein abundances across cells. Rows indicate cells, grouped by cell-state, columns indicate (phospho-)proteins, grouped by cell-state or signaling-state markers. The signaling-state markers, which were not used in the cell-state identification, nonetheless show strong cell-state dependent expression patterns. *D*, multiclass confusion matrix showing the performance of a logistic-regression classifier in predicting the cell-state cluster identity of cells, based on cell-state markers (*left*) or signaling-state markers that were not used in the cell-state assignment (*right*). Performance was assessed in a 5-fold nested cross-validation loop.

co-assignment of cells in the same cluster is determined (Fig. S4, *B* and *C*). Using this approach >98% of the cells were unambiguously assigned (i.e. consistently assigned into the same stable cluster in all 5 iterations, Fig. S4*D*). Moreover, the treatment groups were relatively well distributed over the different clusters, indicating that cluster assignments were not strongly influenced by treatment effects (Fig. S4*E*). Some of these cell-states are associated with specific cell-cycle stages, as evidenced by their levels of Cyclin B1 and Histone H3S10 phosphorylation (Figs. 2*B* and S5*D*), whereas other clusters express keratinocyte basal/progenitor cell marker TP63 (Fig. 2*B*), allowing a degree of biological interpretation to the identified cell-state clusters. Therefore, the 9 stable clusters we identified reflect underlying cell-states prior to treatment.

To explore potential associations between these cell-states and signaling activity we visualized the dataset in a heatmap grouped by cell-state, re-affirming their cluster-associated expression patterns (Fig. 2*C*). Interestingly, the signaling-state markers also exhibited strong cluster dependent patterns (e.g. phospho-LRP6 and Notch Intracellular Domain (NICD)), although these (phospho-)proteins were not used for cell-state identification (Fig. 2, *B* and *C*). This indicates that the identified cell-states capture biological distinctions that are also associated with specific signaling pathway activities. To quantify the extent to which the signaling markers contain information about the cell-state in a more objective way, we trained Machine Learning classifiers (Multinomial Logistic Regression (MLR), Random Forest (RF) and Support Vector Machine (SVM)) to "predict" the cell-state from the signaling-state markers only. As a control we trained these classifiers on the cell-state markers that were used in the original cell-state assignment. In a nested 5-fold cross-validation loop, MLR reached ~88% classification accuracy (Figs. 2*D* and S5*C*). RF and SVM classifiers reached average accuracies of ~81% and ~87%, respectively (Fig. S5, *A*–*C*). When trained

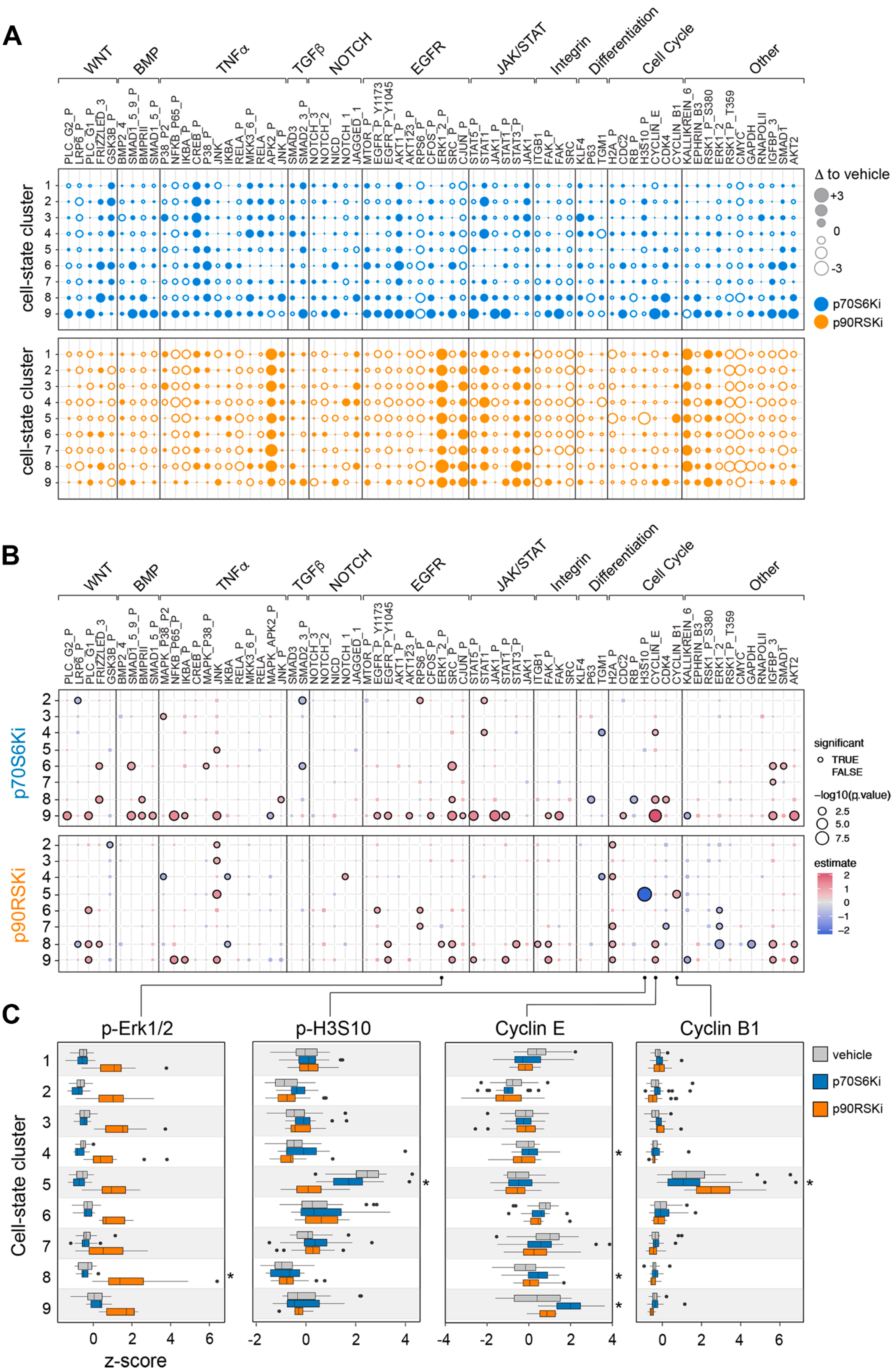

FIG. 3. **Cell-state-specific responses are pervasive and drug dependent.** *A*, differential (phospho-)protein abundance in cells treated with vehicle versus p70S6Ki (*blue*) or p90RSKi (*orange*). Open and closed circles indicate down- and upregulated levels, respectively. *B*, overview of cell-state specific drug response for all cell-state (phospho-)protein pairs, as assessed by a linear model with an interaction

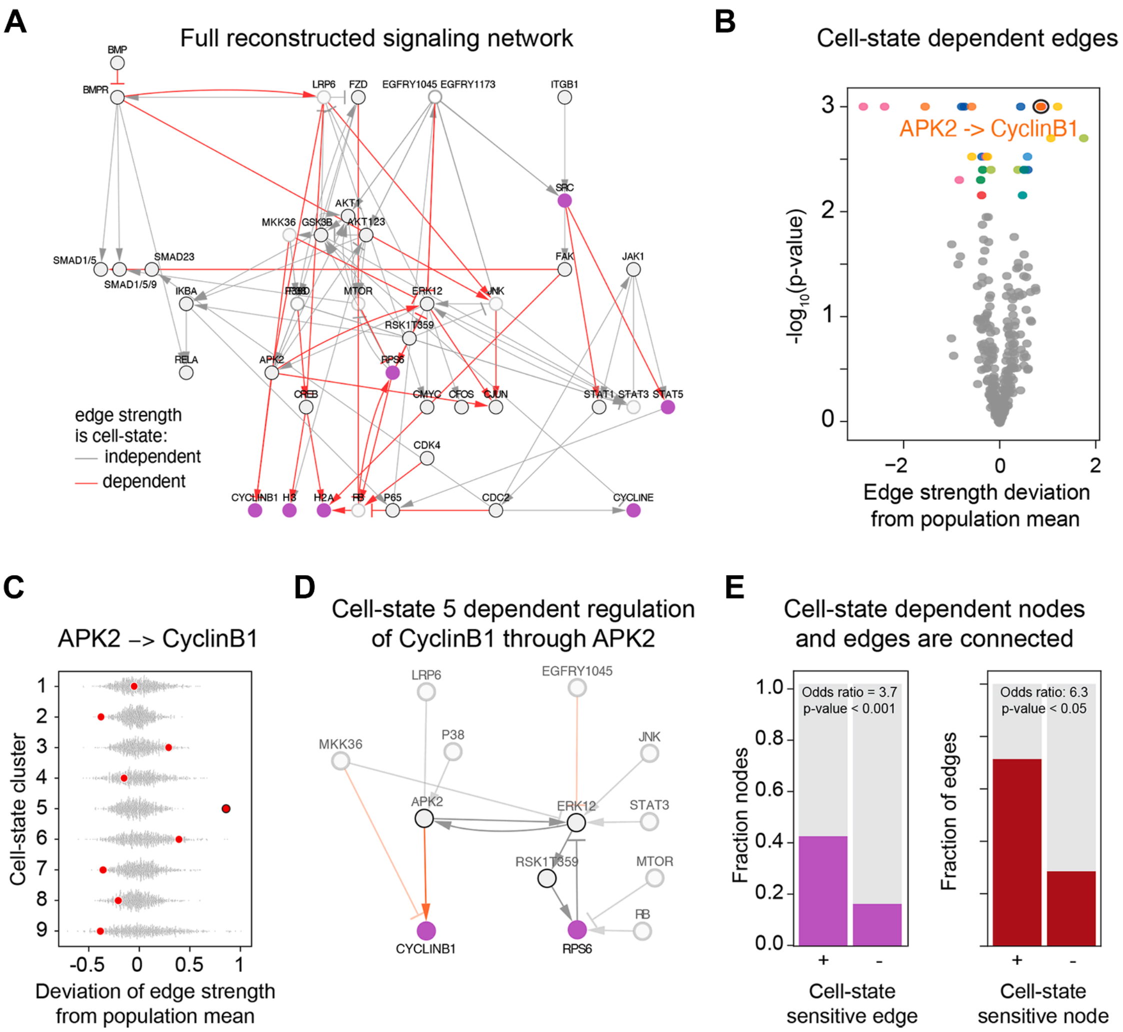

Fig. 4. **Cell-state specific signal transduction and drug response are tightly connected.** *A*, full reconstructed signaling network. *Red* edges indicate Interactions that quantitatively differ between cell-states. *Purple* nodes are (phopsho-)proteins that show cell-state specific drug response. *B*, volcano plot showing the -$\log_{10}$*p*-value and interaction strength deviation from the population mean for all edges that were reconstructed to be cell-state specific (*red* edges in panel a) and all cell-states. The null distribution was obtained by randomly permuting the cell-state labels and reoptimizing the interaction strengths. Interaction-cell-state pairs that are significantly different in a particular cell-state from the population mean are highlighted color, corresponding to the same color code as in Figure 2*A*. *C*, example of an edge (from APK2 to Cyclin B1) whose strength deviates significantly from the population mean, specifically in cell-state 5. *Red* points indicate the true reconstructed edge strengths, *gray dots* represent strengths from reconstructions where the cell-state labels were randomly permuted. In most cell-states, the interaction from APK2 to Cyclin B1 is nearly absent, but in cell-state 5 it is a strong, positive interaction. *D*, highlighted part of the full network that explains the strong cell-state dependence of Cyclin B1 expression. The reduction in RPS6 upon RSKi causes feedback activation of ERK1/2, which in turn activates APK2. Due to the cell-state specific interaction between APK2 and Cyclin B1, only in cell-state 5 does this activation of APK2 translate into an accumulation of Cyclin B1. *E*, visual representation of the contingency tables describing the connection between cell-state dependent drug response and interaction strengths. *Left panel*: The bars indicate the fractions of the nodes that show cell-state dependent drug response, separated by whether or not they have an income edge that has a cell-state dependent strength. *Right panel*: Fraction of edges that have a cell-state dependent strength, separated by whether or not they connect (upstream or downstream) to a node showing cell-state dependent drug response.

---

term, where cell-state 1 was used as a reference. Colors indicate the effect size of the interaction term coefficient, point size indicates the -$\log_{10}$ *p*-value. Significant interactions (*p*-value <0.05) are indicated by a *black* outline. *C*, boxplots of the abundance of Cyclin B1, Cyclin E, phospho-ERK1/2 and phopsho-H3S10, split out per treatment and cell-state cluster, to exemplify cell-state dependent drug-responses. Cell-states with significantly different drug-responses are indicated with an *asterisk*.

on the signaling-state markers in the same nested cross-validation setting, MLR consistently obtained 51% accuracy of predicting the true cell-state labels (Figs. 2*D* and S5*C*). In contrast, an MLR classifier trained on data with randomized labels only reached ~12% accuracy, as expected based on chance (Fig. S5*C*). Similar results were obtained using RF and SVM classifiers (Fig. S5, *B* and *C*). Together, these analyses show that the identified cell-states contain additional intrinsic underlying differences in signaling activities that potentially influence eventual treatment effects of cells in these states.

Cell-State-Dependent Drug Responses are Pervasive and Specific

Our experimental design and analyses thus far also enable us to investigate cell-state dependence of treatment responses. For instance, if the effect of inhibiting p70S6K or p90RSK is independent of cell-state, we would expect treatment-effects to be the same, or at least highly similar, across the identified clusters. In contrast, we observed a high degree of variation of the effects sorted by either inhibitor among the cell-state clusters for individual (phospho-)proteins, as well as at the level of pathway activity scores (Figs. 3*A* and S6, *A* and *B*). To statistically test the extent to which the signaling markers show cell-state-dependent responses to the drug treatments, we fitted a linear regression model that aims to explain (phospho-)protein abundance using drug-treatment, cell-state, and an interaction term between these, for each measured (phospho-)protein. In such models, the interaction term quantifies the extent to which the abundance of a (phospho-)protein in a cell differs from what would be expected based on the drug perturbation and the cell-state separately. We assessed the significance of the interaction term both by using an ANOVA and by considering the coefficients from the linear model directly (Fig. 3*B* and Table S3). The latter approach has the benefit that each interaction between each cell-state-drug treatments is assessed but has the limitation that it requires a reference for the linear regression analysis. Although vehicle control could be used as a logical reference for the treatment, there was no obvious reference with regard to cell-state. We opted to use cell-state 1 as the reference and confirmed that using any of the other cell-states as reference yielded consistent results (Fig. S7*A*). This analysis revealed 100 significant cell-state-dependent treatment responses involving 50 out of the 69 analyzed (phospho-)proteins, across all 8 cell-states (other than the reference cell-state 1) and both inhibitors (*p*-value<0.05, Figs. 3*B*, S7*B* and Table S3). Examples include the specific upregulation of cyclinB1 and downregulation of histone H3S10 phosphorylation levels in cluster 5. Additionally, Cyclin E displays a strong positive interaction between p70S6K inhibition and cell-state 9 (Fig. 3, *B* and *C*). In contrast, ERK1/2 phosphorylation is an example of a phospho-protein that shows cell-state independent, inhibitor treatment specific response (Fig. 3, *B* and *C*). To examine whether cell-state dependent responses propagate through the signaling network, we returned to the analyses of pathway cross-influence based on the activity scores and systematically calculated the change in coefficient of determination among pathways between vehicle and treated cells within each cell-state cluster. This revealed major differences in how pathways influence each other across the different clusters (Fig. S6*C*). Overall, our analyses identified cell-state specific drug-responses that may result from underlying differences in signaling network wiring.

Single-Cell Comparative Network Reconstruction Reveals Cell-State-Specific Signaling Flow and Network Wiring

To quantitatively investigate differences in signaling network wiring between cell-states, we developed single-cell Comparative Network Reconstruction (scCNR). scCNR is designed to exploit the within cell-state variation in signaling activities of the network nodes to quantify their interaction strengths and is described in more detail elsewhere (33). In short, the interaction strength r_{ij} is defined as the percent change in activity of node i upon a 1% change in activity of node j, if all other nodes were to be kept constant. scCNR fits a model with the same topology (i.e., which interactions are present and absent) for each cell-state, but allows for differences in interaction strengths between states. Importantly, our method can take prior information about network topology as an input but can also suggest additional interactions if these significantly improve the model fit. By penalizing the number of interactions in the network, a balance between model complexity and data fit is ensured. Similarly, by penalizing the number of interactions that differ in strength between the cell-states, the most relevant differences in the signaling network between the cell-states are obtained. First, we established a high confidence topology for our network based on literature-derived canonical interactions (see also Fig. S3) and interactions obtained from the public phosphosite plus database (35). Subsequently, we varied the penalty on model complexity to examine the extent to which the model fit could be improved by including extra edges. Adding 34 edges resulted in a good balance between model fit and complexity (Fig. S8, *A* and *B*). Some care needs to be taken in the interpretation of these additional edges, as some may comprise indirect interactions mediated e.g. through additional unobserved nodes. To validate the output topology from our model, we compared it to 1000 models with random topologies (but with the same total number of edges) and quantified model performance as the root mean square of residuals (RMSR). The RMSR of our network model is significantly smaller and falls well outside the distribution of RMSRs from the 1000 random models (*p*-value <0.001, Fig. S8*C*).

Having established the performance of our network reconstruction model, we set out to identify network interactions whose strength differs between cell-states. Using a penalty on the difference between cell-states that gives a sensible balance between the number of differences and model fit (Fig. S8*D*), our scCNR algorithm highlighted 31 edges that account for most of the cell-state specific signaling flow (Fig. 4*A*). Combined, these 31 cell-state specific interaction strengths attain 79% of the total reduction in RMSR that can be gained from cell-state specific edges (Fig. S8*D*). We assessed the robustness of the identification of cell-state-specific edge strength using a bootstrapping experiment, which showed that the majority of cell-state-specific edges are identified in the majority of all bootstraps (Fig. S8*E*). To identify for which edge-cell-state combinations these effects are most important, and to assess the statistical significance of these differences, we performed permutation analyses in which we randomized cell-state assignments while preserving the number of cells from each treatment in each cell-state. We then optimized the edge-strengths while retaining the network topology, and fixing which edges differ between cell-states. We repeated this procedure 1000 times to obtain a null-distribution and an empirical *p*-value of the cell-state dependence of each edge in the network. This identified 22 significant cell-state edge pairs that were different between cell states, which were fairly evenly distributed over the different cell-states (FDR <0.05, Table S4).

The notion that cell-state, drug response, and network effects are interwoven is exemplified by the response of Cyclin B1 to p90RSKi. As discussed above, the inhibition of p90RSK resulted in accumulated phospho-Erk1/2 levels, presumably through a negative feedback loop (49, 50), which in turn leads to APK2 activation (Figs. 1*D*, S1*A* and S2). Our network reconstruction results expand on this and suggest a (potentially indirect) cell-state-dependent interaction where APK2 activation explains Cyclin B1 accumulation specifically in cell-state 5, but not in any of the other cell-states (Fig. 4, *C* and *D*). This is corroborated by the clear cell-state 5-dependent correlation between phospho APK2 and Cyclin B1 (Fig. S8*F*). Indeed, high levels of cell-cycle markers phospho-H3S10 and CyclinB1 in vehicle-treated cells confirm that cells in state 5 are undergoing G2/M transition (Figs. 3*C* and S5). Consistent with this, the mitosis specific marker phospho-H3S10 (51), selectively fails to accumulate in cell-state 5 when p90RSK is inhibited (Fig. 3*C*). Although p90RSK2 was historically described to phosphorylate H3S10 downstream of EGF signaling independently of mitosis (52), our findings suggest that p90RSK-mediated APK2 activity prevents cells from completing the G2/M transition, causing prolonged Cyclin B1 accumelation and preventing H3S10 phosphorylation in p90RSK inhibitor treated human keratinocytes.

Importantly, these observations indicate that cell-state specific differences in node response and edge strength (i.e. network wiring) may be closely related. To test this hypothesis, we investigated if edges that differ between cell-states are more likely to be connected to nodes that show cell-state dependent drug response throughout the whole network. Indeed, 42% of edges that differ between the cell-states are connected to nodes with a significant interaction term, whereas only 16% of edges that do not differ between cell-states are, representing significant enrichment (Fig. 4*E* left panel, Fisher exact test: odds ratio = 3.7, $p < 0.001$). Conversely, 71% of nodes with a significant interaction term receive input from an edge that has a cell-state specific strength, in contrast to only 29% of nodes without a significant interaction term (Fig. 4*E* right panel, Fisher exact test: Odds ratio = 6.3, $p < 0.05$). These results also hold in more fine-grained cell-state specific analyses (Fig. S8*G*). Taken together, our scCNR approach revealed that quantitative differences in signaling network wiring are associated with cell-state dependent drug responses.

DISCUSSION

The question of what makes some cells respond to a given signal differently from other cells is central to understanding processes in normal and disease biology, ranging from symmetry breaking and patterning in early development, to the emergence of therapy-resistance in cancer. We approached this question by characterizing intracellular signaling network activities and wiring upon small molecule inhibitor treatment at the level of individual cells using single-cell ImmunoDetection by sequencing (scID-seq). This work revealed several underappreciated aspects of cellular responses to such treatments. First, inhibiting a downstream effector kinase may result in accumulated activity of upstream pathway components, presumably through disruption of feedback loops. Second, this signal can propagate into alternative routes through the intracellular biochemical signaling network, leading to unintended regulation of downstream DNA-binding transcription factors and their subsequent transcriptional programs. Third, we used the multidimensionality of our data to define 9 distinct cell-states present in our cell population, and found that the response to the inhibitor treatment strongly depended on which of these states a cell resided in. Fourth, using a newly developed single-cell Comparative Network Reconstruction method (33), we were able to identify the quantitative differences in signaling network wiring that are associated with these cell-state dependent drug-responses. It is important to reiterate that our computational network reconstruction method cannot ‘invent’ new nodes that were not included in the measurements, and connections may therefore represent indirect interactions. Hence, some care needs to be taken in interpreting individual interactions and mechanisms, as these are computational reconstructions and we consider them to be hypotheses for further study. Nevertheless, a consistent general picture emerges from our analyses where proteins that show cell-state-dependent response to inhibitor treatment are also more likely to be involved in interactions that show quantitative cell-state-dependent differences.

Our work is consistent with previous findings on cell-type differences in oncogenic signaling in colorectal cancer (53, 54) and with the multimodal perception concept put forward by Kramer and Pelkmans (18). Together, this indicates that redirected and cell-state-dependent signal processing may be inherent to the mechanism of action of targeted therapies, and that these effects need to be accounted for when designing therapeutic strategies. One way to achieve this is to devise strategies to coax cells into cell-states in which they will exhibit the desired response to treatment (55) that can take the form of neoadjuvant or combination therapy regimes. However, this will require a detailed understanding of cell-state differences in network wiring, as well as computational models to identify suitable perturbations to achieve this (56). The approaches and results we presented here can provide a framework for such future directions. Additionally, the fact that our work was performed in primary human cells in the absence of transformation by cancer-associated mutations indicates that cell-state-dependent cellular responses are not restricted to cancer contexts and may also shape normal biology.

DATA AND CODE AVAILABILITY

Sequencing data for the scID-seq and scRNA-seq experiments produced for this work are deposited in the Gene Expression Omnibus (GSE300479). Additionally, TMM normalized data are available as supplementary data associated with this manuscript. Data analysis code is available on https://github.com/jessievb/IDseq and https://github.com/evertbosdriesz/scIDseq-CNR.

Supplemental Data—This article contains supplemental data.

Author Contributions—N. K., R. E., T. S., K. W. M., and E. B. formal analysis; N. K. and R. E. data curation; N. K. and T. S. software; N. K., T. S., E. B., and K. W. M. visualization; N. K., R. E., T. S., S. T., and L. F. A. W. writing–review & editing; R. E., T. S., and S. T. methodology; R. E. and S. T. investigation; R. E., L. F. A. W., E. B., and K. W. M. conceptualization; L. F. A. W., E. B., and K. W. M. resources; L. F. A. W., E. B., and K. W. M. supervision; E. B.: software; E. B. and K. W. M. writing–original draft; K. W. M. project administration.

Received August 28, 2025, and in revised form, February 9, 2026
Published, MCPRO Papers in Press, February 16, 2026, https://doi.org/10.1016/j.mcpro.2026.101529

REFERENCES

1. Manning, B. D., and Toker, A. (2017) AKT/PKB signaling: navigating the network. *Cell* **169**, 381–405
2. Mendoza, M. C., Er, E. E., and Blenis, J. (2011) The Ras-ERK and PI3K-mTOR pathways: cross-talk and compensation. *Trends Biochem. Sci.* **36**, 320–328
3. Meyuhas, O. (2015) Ribosomal protein S6 phosphorylation: four decades of research. *Int. Rev. Cell Mol. Biol.* **320**, 41–73
4. Lim, C. P., and Cao, X. (2001) Regulation of Stat3 activation by MEK kinase 1. *J. Biol. Chem.* **276**, 21004–21011
5. Lun, X.-K., Zanotelli, V. R. T., Wade, J. D., Schapiro, D., Tognetti, M., Dobberstein, N., *et al*. (2017) Influence of node abundance on signaling network state and dynamics analyzed by mass cytometry. *Nat. Biotechnol.* **35**, 164–172
6. Krishnaswamy, S., Spitzer, M. H., Mingueneau, M., Bendall, S. C., Litvin, O., Stone, E., *et al*. (2014) Systems biology. Conditional density-based analysis of T cell signaling in single-cell data. *Science* **346**, 1250689
7. Bugaj, L. J., Sabnis, A. J., Mitchell, A., Garbarino, J. E., Toettcher, J. E., Bivona, T. G., *et al*. (2018) Cancer mutations and targeted drugs can disrupt dynamic signal encoding by the Ras-Erk pathway. *Science* **361**, eaao3048
8. Yaffe, M. B. (2019) Why geneticists stole cancer research even though cancer is primarily a signaling disease. *Sci. Signal.* **12**, eaaw3483
9. Weinstein, I. B. (2002) Cancer. Addiction to oncogenes–the achilles heal of cancer. *Science* **297**, 63–64
10. Flaherty, K. T., Infante, J. R., Daud, A., Gonzalez, R., Kefford, R. F., *et al*. (2012) Combined BRAF and MEK inhibition in melanoma with BRAF V600 mutations. *N. Engl. J. Med.* **367**, 1694–1703
11. Long, G. V., Stroyakovskiy, D., Gogas, H., Levchenko, E., de Braud, F., *et al*. (2014) Combined BRAF and MEK inhibition versus BRAF inhibition alone in melanoma. *N. Engl. J. Med.* **371**, 1877–1888
12. Kobayashi, S., Boggon, T. J., Dayaram, T., Jänne, P. A., Kocher, O., *et al*. (2005) EGFR mutation and resistance of non-small-cell lung cancer to gefitinib. *N. Engl. J. Med.* **352**, 786–792
13. Pao, W., Miller, V. A., Politi, K. A., Riely, G. J., Somwar, R., *et al*. (2005) Acquired resistance of lung adenocarcinomas to gefitinib or erlotinib is associated with a second mutation in the EGFR kinase domain. *PLoS Med.* **2**, e73
14. Shaffer, S. M., Dunagin, M. C., Torborg, S. R., Torre, E. A., Emert, B., *et al*. (2017) Rare cell variability and drug-induced reprogramming as a mode of cancer drug resistance. *Nature* **546**, 431–435
15. Goyal, Y., Busch, G. T., Pillai, M., Li, J., Boe, R. H., Grody, E. I., *et al*. (2023) Diverse clonal fates emerge upon drug treatment of homogeneous cancer cells. *Nature* **620**, 651–659
16. Emert, B. L., Cote, C. J., Torre, E. A., Dardani, I. P., Jiang, C. L., Jain, N., *et al*. (2021) Variability within rare cell states enables multiple paths toward drug resistance. *Nat. Biotechnol.* **39**, 865–876
17. Schaff, D. L., Fasse, A. J., White, P. E., Vander Velde, R. J., and Shaffer, S. M. (2024) Clonal differences underlie variable responses to sequential and prolonged treatment. *Cell Syst* **15**, 213–226.e9
18. Kramer, B. A., del Castillo, J. S., and Pelkmans, L. (2022) Multimodal perception links cellular state to decision making in single cells. *Science* **337**, eabf4062
19. Altschuler, S. J., and Wu, L. F. (2010) Cellular heterogeneity: do differences make a difference? *Cell* **141**, 559–563
20. Newberry, E. P., and Pike, L. J. (1995) Cell-cycle-dependent modulation of EGF-receptor-mediated signaling. *Biochem. Biophys. Res. Commun.* **208**, 253–259
21. Kiyokawa, N., Lee, E. K., Karunagaran, D., Lin, S. Y., and Hung, M. C. (1997) Mitosis-specific negative regulation of epidermal growth factor receptor, triggered by a decrease in ligand binding and dimerization, can be overcome by overexpression of receptor. *J. Biol. Chem.* **272**, 18656–18665
22. Gandarillas, A., and Watt, F. M. (1997) c-Myc promotes differentiation of human epidermal stem cells. *Genes Dev.* **11**, 2869–2882
23. van Buggenum, J. A. G., Gerlach, J. P., Tanis, S. E. J., Hogeweg, M., Jansen, P. W. T. C., Middelwijk, J., *et al*. (2018) Immuno-detection by sequencing enables large-scale high-dimensional phenotyping in cells. *Nat. Commun.* **9**, 2384
24. van Eijl, R. A. P. M., van Buggenum, J. A. G. L., Tanis, S. E. J., Hendriks, J., and Mulder, K. W. (2018) Single-cell ID-seq reveals dynamic BMP pathway activation upstream of the MAF/MAFB-Program in epidermal differentiation. *iScience* **9**, 412–422
25. van Buggenum, J. A. G. L., Gerlach, J. P., Eising, S., Schoonen, L., van Eijl, Tanis, S. E. J., *et al*. (2016) A covalent and cleavable antibody-DNA

conjugation strategy for sensitive protein detection via immuno-PCR. *Sci. Rep.* **6**, 22675

26. Gerlach, J. P., van Buggenum, Tanis, S. E. J., Hogeweg, M., Heuts, B. M. H., Muraro, M. J., *et al*. (2019) Combined quantification of intracellular (phospho-)proteins and transcriptomics from fixed single cells. *Sci. Rep.* **9**, 1469
27. Robinson, M. D., McCarthy, D. J., and Smyth, G. K. (2010) edgeR: a bioconductor package for differential expression analysis of digital gene expression data. *Bioinformatics* **26**, 139–140
28. Ritchie, M. E., Phipson, B., Wu, D., Hu, Y., Law, C. W., Shi, W., *et al*. (2015) Limma powers differential expression analyses for RNA-sequencing and microarray studies. *Nucleic Acids Res.* **43**, e47
29. Hashimshony, T., Senderovich, N., Avital, G., Klochendler, A., de Leeuw, Y., Anavy, L., *et al*. (2016) CEL-Seq2: sensitive highly-multiplexed single-cell RNA-Seq. *Genome Biol.* **17**, 77
30. Langmead, B., and Salzberg, S. L. (2012) Fast gapped-read alignment with Bowtie 2. *Nat. Methods* **9**, 357–359
31. Traag, V. A., Waltman, L., and van Eck, N. J. (2019) From Louvain to Leiden: guaranteeing well-connected communities. *Sci. Rep.* **9**, 5233
32. Ahmad, A., and Dey, L. (2007) A k-mean clustering algorithm for mixed numeric and categorical data. *Data Knowl. Eng.* **63**, 503–527
33. Stohn, T., van Eijl, R., Mulder, K. W., Wessels, L. F. A., and Bosdriesz, E. (2025) Reconstructing and comparing signal transduction networks from single-cell protein quantification data. *Bioinformatics* **42**, btaf675
34. Bosdriesz, E., Prahallad, A., Klinger, B., Sieber, A., Bosma, A., Bernards, R., *et al*. (2018) Comparative network reconstruction using mixed integer programming. *Bioinformatics* **34**, i997–i1004
35. Hornbeck, P. V., Zhang, B., Murray, B., Kornhauser, J. M., Latham, V., and Skrzypek, E. (2015) PhosphoSitePlus, 2014: mutations, PTMs and recalibrations. *Nucleic Acids Res.* **43**, D512–D520
36. Karjosukarso, D. W., Dini, A., Wingens, L. J. A., Liu, R., Joosten, L. A. B., Bussink, J., *et al*. (2023) Signalling-state dependent drug-tolerance in head and neck squamous cell carcinoma. *bioRxiv*. https://doi.org/10.1101/2023.12.05.570063
37. Stoeckius, M., Zheng, S., Houck-Loomis, B., Hao, S., Yeung, B. Z., Mauck, W. M., *et al*. (2018) Cell hashing with barcoded antibodies enables multiplexing and doublet detection for single cell genomics. *Genome Biol.* **19**, 224
38. Prahallad, A., Sun, C., Huang, S., Di Nicolantonio, F., Salazar, R., Zecchin, D., *et al*. (2012) Unresponsiveness of colon cancer to BRAF(V600E) inhibition through feedback activation of EGFR. *Nature* **483**, 100–U146
39. Klinger, B., Sieber, A., Fritsche-Guenther, R., Witzel, F., Berry, L., Schumacher, D., *et al*. (2013) Network quantification of EGFR signaling unveils potential for targeted combination therapy. *Mol. Syst. Biol.* **9**, 673
40. Wu, D., and Pan, W. (2010) GSK3: a multifaceted kinase in Wnt signaling. *Trends Biochem. Sci.* **35**, 161–168
41. Markussen, L. K., Winther, S., Wicksteed, B., and Hansen, J. B. (2018) GSK3 is a negative regulator of the thermogenic program in brown adipocytes. *Sci. Rep.* **8**, 3469
42. Abell, A. N., Granger, D. A., and Johnson, G. L. (2007) MEKK4 stimulation of p38 and JNK activity is negatively regulated by GSK3β. *J. Biol. Chem.* **282**, 30476–30484
43. Reyskens, K. M. S. E., and Arthur, J. S. C. (2016) Emerging roles of the mitogen and stress activated kinases MSK1 and MSK2. *Front. Cell Dev. Biol.* **4**, 56
44. Roux, P. P., and Blenis, J. (2004) ERK and p38 MAPK-activated protein kinases: a family of protein kinases with diverse biological functions. *Microbiol. Mol. Biol. Rev.* **68**, 320–344
45. Gough, D. J., Koetz, L., and Levy, D. E. (2013) The MEK-ERK pathway is necessary for serine phosphorylation of mitochondrial STAT3 and Ras-mediated transformation. *PLoS One* **8**, e83395
46. Jain, N., Zhang, T., Fong, S. L., Lim, C. P., and Cao, X. (1998) Repression of Stat3 activity by activation of mitogen-activated protein kinase (MAPK). *Oncogene* **17**, 3157–3167
47. Ben-Levy, R., Leighton, I. A., Doza, Y. N., Attwood, P., Morrice, N., Marshall, C. J., *et al*. (1995) Identification of novel phosphorylation sites required for activation of MAPKAP kinase-2. *EMBO J.* **14**, 5920–5930
48. Angel, P., Hattori, K., Smeal, T., and Karin, M. (1988) The Jun proto-oncogene is positively autoregulated by its product, Jun/AP-1. *Cell* **55**, 875–885
49. Kim, M., Lee, J. H., Koh, H., Lee, S. Y., Jang, C., Chung, C. J., *et al*. (2006) Inhibition of ERK-MAP kinase signaling by RSK during Drosophila development. *EMBO J.* **25**, 3056–3067
50. Myers, A. P., Corson, L. B., Rossant, J., and Baker, J. C. (2004) Characterization of mouse Rsk4 as an inhibitor of fibroblast growth factor-RAS-extracellular signal-regulated kinase signaling. *Mol. Cell Biol.* **24**, 4255–4266
51. Hans, F., and Dimitrov, S. (2001) Histone H3 phosphorylation and cell division. *Oncogene* **20**, 3021–3027
52. Sassone-Corsi, P., Mizzen, C. A., Cheung, P., Crosio, C., Monaco, L., Jacquot, S., *et al*. (1999) Requirement of Rsk-2 for epidermal growth factor-activated phosphorylation of histone H3. *Science* **285**, 886–891
53. Sell, T., Klotz, C., Fischer, M. M., Astaburuaga-García, R., Krug, S., Drost, J., *et al*. (2023) Oncogenic signaling is coupled to colorectal cancer cell differentiation state. *J. Cell Biol.* **222**
54. Uhlitz, F., Bischoff, P., Peidli, S., Sieber, A., Trinks, A., Lüthen, M., *et al*. (2021) Mitogen-activated protein kinase activity drives cell trajectories in colorectal cancer. *EMBO Mol. Med.* **13**, e14123
55. Rukhlenko, O. S., Halasz, M., Rauch, N., Zhernovkov, V., Prince, T., Wynne, K., *et al*. (2022) Control of cell state transitions. *Nature* **609**, 975–985
56. Bosdriesz, E., Fernandes Neto, Sieber, A., Bernards, R., Blüthgen, N., and Wessels. (2022) Identifying mutant-specific multi-drug combinations using comparative network reconstruction. *iScience* **25**, 104760